Inorganic Chemistry

Article

Cite This: Inorg. Chem. 2019, 58, 3425−3434

pubs.acs.org/IC

Organic Compounds of Actinyls: Systematic Computational Assessment of Structural and Topological Properties in $[AnO_2(C_2O_4)_n]^{(2n-2)-}$ (An = U, Np, Pu, Am; n = 1−3) Complexes

Meigang Duan,[†] Peng Li,*[,†] Huifeng Zhao,[†] Feng Xie,[‡] and Jie Ma[†]

[†]Laser Spectroscopy Laboratory, School of Physics and Electronics Engineering, Collaborative Innovation Center of Extreme Optics, Shanxi University, Taiyuan 030006, China

[‡]Institute of Nuclear and New Energy Technology, Collaborative Innovation Center of Advanced Nuclear Energy Technology, Key Laboratory of Advanced Reactor Engineering and Safety of Ministry of Education, Tsinghua University, Beijing 100084, China

Supporting Information

ABSTRACT: Exploring the bonding features between organics and actinide elements is a fundamental topic in nuclear waste separation. In this work, $[AnO_2(C_2O_4)_n]^{(2n-2)-}$ (An = U, Np, Pu, and Am; n = 1−3) complexes have been characterized by density functional theory. The actinyl oxalate complexes are found to exhibit the typical An−O_{yl}, An−O_{eq} bonds and O_{yl}−An−O_{yl} angles. Interatomic interaction analyzed by electron density difference, charge decomposition analysis, charges population, bond order, electron localization function, and quantum theory of atom in molecules indicates that An−O_{eq} bonds are ionic (closed-shell) bonding interaction with a small degree of covalent character. The similarities and differences between isomers have been discussed in the actinide coordination chemistry, and the orbital interactions also have been investigated through total, partial, and overlap population density of state diagrams. Besides, the electrostatic potential was used to predict the adsorption sites on the molecular vdW surface.

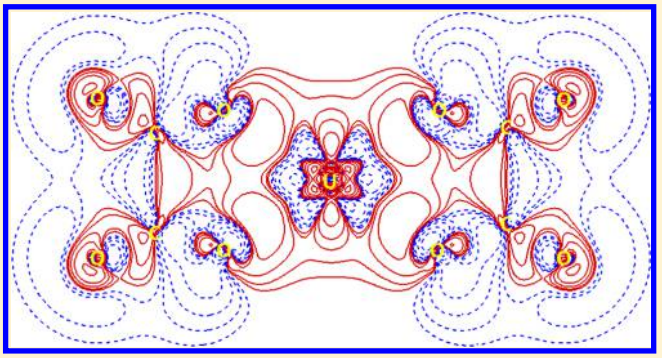

1. INTRODUCTION

The nuclear energy produced by uranium fission currently may be one of the most perfect replacements for fossil fuel energy, but this task represents a tremendous challenge for further development. Up to now, how to effectively, safely, and economically utilize used spent nuclear fuel is still in the technical exploration stage.[1−5] Furthermore, the spent fuel mainly includes ^{235}U, ^{239}Pu, some minor actinides (Np, Am, Cm) and their fission products (^{90}Sr, ^{137}Cs, ^{99}Tc, etc.) in the aqueous environment.[6] The separation of the spent fuel is also a severe issue in the subsequent waste managing processes.

Due to the complexity of *5f* and *6d* orbital electrons, actinide elements have more valence states (+4, +5, +6, and +7),[7] and the hexavalent oxidation is more accessible. The actinyl AnO_2^{2+} is capable of greatly interfacing with some organic ligands, particularly interaction with O-donor ligands, which can form metal−organic complexes. Studies have shown that these complexes can be effectively used to extract actinides and highly radioactive fission products from spent fuel.[8,9] In addition, it is also an important topic to study the interaction between unpaired *5f* electrons and *p*-electrons of ligands.

These metal−organic complexes are the building blocks of the metal−organic frameworks (MOFs) material.[10−14] Because the uranyl-organic frameworks (UOFs) have potential applications in the post-treatment of spent fuel, it is one of the most investigated porous solid materials compared with other MOFs.[15−18] Recently, Wang et al. have reported a new class of pentagonal bipyramidal uranyl materials, the five equatorial oxygens provided by two oxalate groups and one carboxylate ligand, and it is substantially stabilized under radiation fields.[19] They discovered that oxalate-carboxylate as the coordinating ligands can directly interact with hexavalent uranyl ions. Besides, experimental studies indicate that UOFs have the advantages of highest surface area and controllable pore size. More impressively, UOFs can selectively eliminate radioactive ^{90}Sr and ^{137}Cs cations, which provides convenience for further partitioning of nuclear waste and emergency remediation.

The experimental results of the above UOFs materials provide intuitive information for further research. Nevertheless, the crucial microscopic interaction mechanism and electronic structure between AnO_2^{2+} and ligands cannot be directly available from the experiment. At the same time, the development of theoretical calculation provides a powerful tool for the above problems.[20−26] In recent years, Li and Gibson et

Received: December 20, 2018
Published: February 20, 2019

DOI: 10.1021/acs.inorgchem.8b03538
Inorg. Chem. 2019, 58, 3425−3434

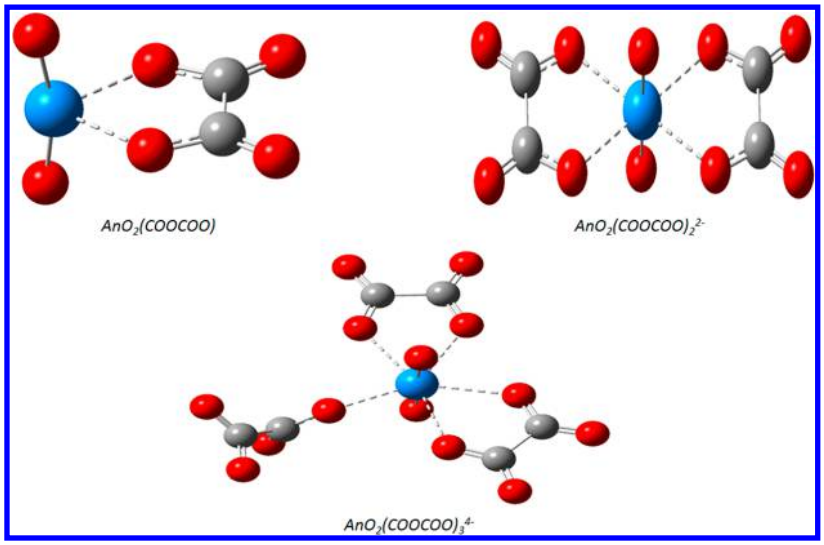

Figure 1. Optimized geometries of $[AnO_2(C_2O_4)_n]^{(2n-2)-}$ complexes using PW91-ZORA/def2-TZVPP-SARC and B3LYP-ZORA/def-TZVPP-SARC.

al. have determined the geometries, binding mechanisms, and orbital interactions of the complexes $[AnO_2(15C5)]^{2+}$ and $[AnO_2(L)_n]^{2+}$ (An = U, Np, Pu, Am, and Cm; n = 1, 2; L = 12TC4, 15TC5, and 18TC6) by using density functional theory (DFT).[27,28] Su et al. showed that the ionic and covalent interactions exist in uranyl and carboxylates ligands.[14] Their results indicated that there are obvious periodic trends in the chemistry of the actinides. Not only that, these theoretical studies have verified that DFT is a universal and successful method for the calculation of actinyl organic complexes.

In this study, an in-depth exploration of the gas-phase $[AnO_2(C_2O_4)_n]^{(2n-2)-}$ (n = 1−3) complexes (An = U−Am) using DFT has been performed. The main focus lies in detecting the electronic state and microscopic interaction of these complexes. The bonding characteristic and topological properties have been analyzed by the quantum theory of atom in molecules (QTAIM). In addition, the reactivity analysis by using electrostatic potential (ESP) on molecular vdW surface has been performed to predict the adsorption sites of fission product cations.

2. COMPUTATIONAL METHODS

All density functional theory (DFT) calculations of the $[AnO_2(C_2O_4)_n]^{(2n-2)-}$ complexes were performed with the ORCA-4.0.1 package.[29] The geometry optimization and frequency calculations were carried out using the PW91[30] and B3LYP[31] methods. The geometry optimizations were endowed without symmetry restrictions. The single-point energies were calculated using PWPB95[32] with the Grimme's atom-pairwise dispersion correction and Becke−Johnson damping (D3BJ)[33] based on PW91 geometries. The segmented all-electron relativistically contracted (SARC)[34] was applied for U, Np, Pu, and Am, and the triple-ζ valence basis sets (def2-TZVPP[35] and def2-TZVPPD[36]) were used for the light C and O atoms. The scalar relativistic effect was examined using the zero-order regular approximation (ZORA)[37] and Douglas−Kroll−Hess Hamiltonian of second order (DKH2).[38,39] The binding energy analyses were carried out using the PW91-ZORA/def2-TZVPPD and PW91-DKH2/def2-TZVPPD. The conductor-like screening solvation model (COSMO)[40] was employed to consider the effects of solvation. The zero-point vibrational energy and thermal corrections were taken into account. It could be important to research the spin−orbit effects for the actinyl ions due to their open-shell ground state; however, the contributions of the spin−orbit effects are constant with the addition of ligands.[41,42] Therefore, there are not significant effects on the sequential energies, so spin−orbit effects were not treated in this study. Time-dependent density functional theory (TD-DFT) was implemented to calculate the excited states including 10 transitions with the PW91-ZORA/def2-TZVPP-SARC level.

The bonding natures were analyzed with the MULTIWFN program[43] based on the all-electron wave functions obtained at the PW91-ZORA/def2-TZVPP-SARC level of theory. The electron density difference and charge decomposition analysis (CDA)[44] were performed to unveil the detail of charge transfer between the AnO_2^{2+} and $(C_2O_4)^{2-}$. The Hirfsheld atom population[45] and Voronic deformation density (VDD) atom population[46] were carried out. Bond order analyses were using the Mayer bond order (MBO)[47] and Fuzzy bond-order (FBO) methods.[48−51] The topological properties analyses were conducted by the electron localization function (ELF)[52] and QTAIM theory.[53] Total, partial, and overlap population density of state (TDOS, PDOS, and OPDOS)[54,55] analyses were used to gather the information on orbital interaction. Furthermore, the ESP[56] on the molecular vdW surface was used to predict the adsorption sites.

3. RESULTS AND DISCUSSION

3.1. Structures and Electronic Properties of the $[AnO_2(C_2O_4)_n]^{(2n-2)-}$. In order to find the low-lying energy structures, extensive possible initial conformations of $[AnO_2(C_2O_4)_n]^{(2n-2)-}$ complexes (An = U−Am; n = 1−3) were searched, and the different possible spin multiplicities were considered two theoretical levels (PW91-ZORA/def2-TZVPP-SARC and B3LYP-ZORA/def-TZVPP-SARC). These ground state geometries are shown in Figure 1. Since one spin state can have plenty of low-lying excited states in the case of actinides, we have checked all the optimized structures by TD-DFT and the corresponding results have been listed in the Supporting Information (Table S1 and Table S2). As can be seen, all excitation energies are positive indicating that the initial state is more stable than the excited states. The detailed Cartesian coordinates of the ground state $[AnO_2(C_2O_4)_n]^{(2n-2)-}$ complexes (An = U−Am; n = 1−3) were given in Table S3.

It can be seen that the three actinide complexes have similar structures. The AnO_2^{2+} prefers coordination by the O atoms of $C_2O_4^{2-}$ on the equatorial plane (O_{eq} represents the $C_2O_4^{2-}$ oxygen atoms, O_{yl} represents the AnO_2^{2+} oxygen atoms).

DOI: 10.1021/acs.inorgchem.8b03538
Inorg. Chem. 2019, 58, 3425−3434

Table 1. Selected Average Bond Length (Å) and O_{yl}–An–O_{yl} Bond Angle (deg) of the Ground-State $AnO_2(C_2O_4)$, $[AnO_2(C_2O_4)_2]^{2-}$, $[AnO_2(C_2O_4)_3]^{4-}$, and Isomers in Vacuum and in Water Using the COSMO Solvation Model (in Parentheses) at PW91-ZORA/def2-TZVPP-SARC

		$AnO_2(C_2O_4)$			$AnO_2(C_2O_4)_2^{2-}$			$AnO_2(C_2O_4)_3^{4-}$			ISOMERS		
		Bond length		Bond angle	Bond length		Bond angle	Bond length		Bond angle	Bond length		Bond angle
An	2S+1	An–O_{yl}	An–O_{eq}	O_{yl}–An–O_{yl}	An–O_{yl}	An–O_{eq}	O_{yl}–An–O_{yl}	An–O_{yl}	An–O_{eq}	O_{yl}–An–O_{yl}	An–O_{yl}	An–O_{eq}	O_{yl}–An–O_{yl}
U	1	1.792 (1.784)	2.156 (2.213)	165.0 (172.9)	1.819 (1.817)	2.331 (2.330)	179.9 (179.9)	1.822 (1.826)	2.453 (2.391)	176.8 (179.3)	1.811 (1.813)	2.552 (2.489)	179.9 (179.9)
Np	2	1.772 (1.765)	2.155 (2.207)	172.5 (176.8)	1.799 (1.797)	2.321 (2.318)	179.9 (179.9)	1.802 (1.805)	2.459 (2.387)	177.6 (179.5)	1.790 1.791)	2.552 (2.486)	179.7 (179.6)
Pu	3	1.768 (1.753)	2.352 (2.224)	176.9 (178.1)	1.787 (1.783)	2.325 (2.324)	180.0 (179.9)	1.792 (1.789)	2.486 (2.394)	178.1 (179.0)	1.783 (1.783)	2.557 (2.487)	179.6 (179.6)
Am	4	1.768 (1.744)	2.365 (2.243)	177.8 (179.6)	1.780 (1.774)	2.324 (2.324)	180.0 (179.9)	1.789 (1.781)	2.507 (2.391)	178.7 (179.3)	1.780 (1.779)	2.565 (2.487)	179.9 (179.9)

These structures can be vividly described as tetrahedron, octahedron, and pentagonal bipyramidal, respectively. In view of the fact that these complexes are predominantly in the form of ions and usually exist in aqueous, the COSMO model was considered in optimization to represent polarizable water solvent.

The detailed geometric parameters of the ground state at PW91-ZORA/def2-TZVPP-SARC are presented in Table 1; the results of other methods are displayed in Table S4. We can see that the solvation has little influence on the geometric parameters; this property also appears in previous studies of similar systems.[25,26] Therefore, the following discussion only corresponds to the gas phase.

Figure 2 intuitively shows the variation of bonds lengths and bond orders for An–O_{eq} and An–O_{yl} bonds. The average length of An–O_{yl} bonds decreases from U (1.792 Å, 1.819 and 1.822 Å) to Am (1.768, 1.780, and 1.789 Å); the decreased trend is consistent with the An–O_{yl} bond lengths in isolated actinyl, as expected due to the contraction of the actinide ionic radius. The bond lengths of An–O_{eq} in $[AnO_2(C_2O_4)_3]^{4-}$ exceed the range of An–O single-bond covalent radii provided by Pyykkö,[57] which indicates that such chemical bonds are primarily coordination interactions. The average lengths of the An–O_{eq} increase from U (2.453 Å) to Am (2.507 Å) for $[AnO_2(C_2O_4)_3]^{4-}$, possibly due to contraction of the *5f*/*6d* orbitals. Besides, as the number of $(C_2O_4)^{2-}$ increases, the average distances of the An–O_{eq} bond increased from $[AnO_2(C_2O_4)]$ (2.156 and 2.155 Å) to $[AnO_2(C_2O_4)_3]^{4-}$ (2.453 and 2.459 Å) for U and Np cases. Based on the increasing An–O_{eq} bond lengths a weaker bonding interaction between the An and O_{eq} might be deceptive; it is notable that the BEs (Table 2) suggest a decreasing tread in bonding between the $(AnO_2)^{2+}$ (U and Np) and $(C_2O_4)^{2-}$ with the $(C_2O_4)^{2-}$ ligands increasing. This indicates that the interaction between An and O_{eq} in $[AnO_2(C_2O_4)_3]^{4-}$ is weaker than that in $[AnO_2(C_2O_4)]$. This can also be supported by Mayer bond order and Fuzzy bond order analysis (Table S5).

For the case of Pu and Am, the average An–O_{eq} distances change with the trend of $AnO_2(C_2O_4)$ > $[AnO_2(C_2O_4)_2]^{2-}$ < $[AnO_2(C_2O_4)_3]^{4-}$. By contrast, we find that the change trend of An–O_{eq} length is different for U, Np and Pu, Am. The Pu–O_{eq} and Am–O_{eq} bond lengths in $AnO_2(C_2O_4)$ are longer than in $[AnO_2(C_2O_4)_2]^{2-}$. This unique phenomenon is possibly ascribed to their unstable structure and different coordination. In addition, the distances of the An–O_{eq} bond in $[AnO_2(C_2O_4)]$ and $[AnO_2(C_2O_4)_2]^{2-}$ complexes decrease from U (2.156 and 2.331 Å) to Np (2.155 and 2.321 Å) and then increase to Pu (2.352 and 2.325 Å). This transition phenomenon also occurred in the $[AnO_2(15C5)]^{2+}$ and $[AnO_2(L)_n]^{2+}$ (An = U, Np, Pu, Am, and Cm; n = 1, 2; L = 12TC4, 15TC5, and 18TC6) complexes.[58−61] The change in O≡An≡O bond angles from highly bent for U to linear for Am is partially attributed to steric repulsion and electrostatic factors between ligands and actinyls ions.

3.2. Chemical Bonding Characterizations Analyses of $[AnO_2(C_2O_4)_n]^{(2n-2)-}$. The Hirfsheld and Voronoi deformation density (VDD) charges were listed in Table 3. As can be seen, the solvation has little effect on charge population. The An (An = U–Am) center carries a high positive charge, and the O_{eq} ligands carry large negative charges in these complexes.

In order to obtain a deep insight into the nature of the charge transformation, we performed the contour plots of electron density difference and charge decomposition analysis

DOI: 10.1021/acs.inorgchem.8b03538
Inorg. Chem. 2019, 58, 3425−3434

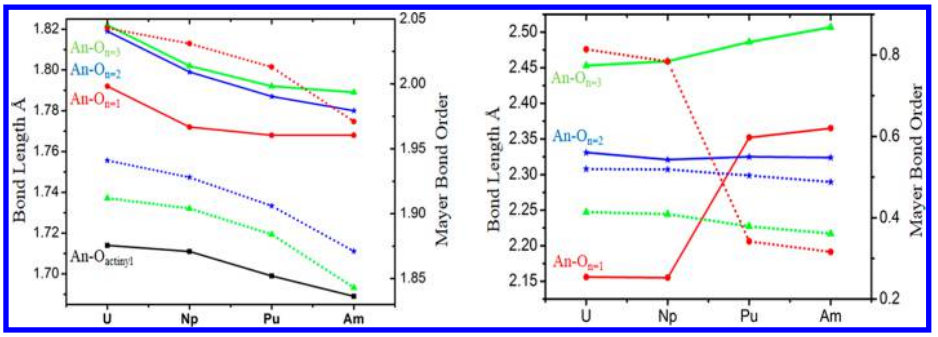

Figure 2. Left: mean An−O_{yl} bond distance (solid lines, left axis) and An−O_{yl} bond order (dotted lines, right axis) of isolated AnO_2^{2+} (black squares), $AnO_2(COOCOO)$ (red circles), $AnO_2(COOCOO)_2^{2-}$ (blue stars), and $AnO_2(COOCOO)_3^{4-}$ (green triangles). Right: mean An−O_{eq} bond distance (solid lines, left axis) and An−O_{eq} bond order (dotted lines, right axis) of $AnO_2(COOCOO)$ (red circles), $AnO_2(COOCOO)_2^{2-}$ (blue stars), and $AnO_2(COOCOO)_3^{4-}$ (green triangles).

Table 2. Binding Energy (BE, kcal/mol) Defined as $AnO_2^{2+} + n(L)^{2-} \rightarrow [AnO2(L)_n]^{(2n-2)-}$ (L = (C_2O_4), n = 1−3) at PW91/def2-TZVPPD with ZORA and DKH2

	$AnO_2(C_2O_4)$		$AnO_2(C_2O_4)_2^{2-}$		$AnO_2(C_2O_4)_3^{4-}$	
An	ZORA	DKH2	ZORA	DKH2	ZORA	DKH2
U	−310.9	−274.2	−247.1	−246.9	−242.7	−242.5
Np	−303.4	−302.8	−244.1	−244.9	−239.3	−239.5
Pu	−304.7	−260.1	−243.0	−243.0	−236.6	−236.8
Am	−307.2	−306.2	−242.5	−242.5	−235.6	−235.2

(CDA); the results of $[UO_2(C_2O_4)_n]^{(2n-2)-}$ complexes were displayed in Figure 3 and Figure 4, respectively. The correlative figures for other complexes are shown in the Supporting Information (Figure S1 and Figure S2). As can be seen from Figure 3, the contour regions are convex from O_{eq} to U, which represents the charge transfer from O_{eq} to U. In Figure 4, the HOMOs of $[UO_2(C_2O_4)_n]^{(2n-2)-}$ complexes primarily contain the orbitals of $(C_2O_4)^{2-}$. Therefore, the electron transitions occurred in the $(C_2O_4)^{2-}$. The above charge transfer analysis indicates that for An−O_{eq} there exists ionic interactions with weak covalence.

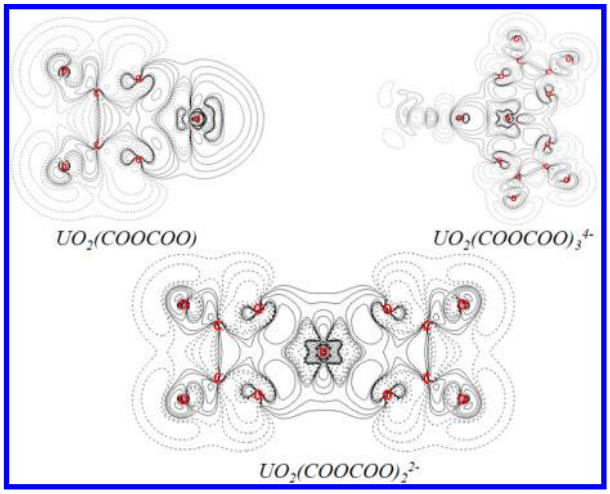

Figure 3. Contour plots of the electron density difference between UO_2^{2+} and $n(C_2O_4)^{2-}$ (n = 1−3) fragments. Solid lines represent regions where electron density increases, and dotted lines represent the region where the electron density decreases.

Table 3. Hirfsheld and VDD Charges for An, O_{yl}, and O_{eq} in the $[AnO_2(C_2O_4)_n]^{(2n-2)-}$ and Isomers in Vacuum and in Water Using the COSMO Solvation Model (in Parentheses) at PW91-ZORA/def2-TZVPP-SARC

	Hirfsheld Charges			VDD Charges		
Complexes	Q(An)	Q(O_{yl})	Q(O_{eq})	Q(An)	Q(O_{yl})	Q(O_{eq})
$UO_2(C_2O_4)$	1.067 (1.272)	−0.310 (−0.305)	−0.214 (−0.217)	0.673 (0.854)	−0.190 (−0.173)	−0.160 (−0.159)
$UO_2(C_2O_4)_2^{2-}$	0.657 (0.704)	−0.384 (−0.389)	−0.259 (−0.260)	0.476 (0.492)	−0.393 (−0.394)	−0.233 (−0.230)
$UO_2(C_2O_4)_3^{4-}$	0.541 (0.491)	−0.392 (−0.412)	−0.258 (−0.276)	0.498 (0.478)	−0.423 (−0.448)	−0.258 (−0.283)
$NpO_2(C_2O_4)$	0.985 (1.183)	−0.290 (−0.281)	−0.201 (−0.206)	0.617 (0.781)	−0.180 (−0.155)	−0.148 (−0.148)
$NpO_2(C_2O_4)_2^{2-}$	0.581 (0.620)	−0.360 (−0.362)	−0.252 (−0.253)	0.400 (0.413)	−0.364 (−0.436)	−0.227 (−0.225)
$NpO_2(C_2O_4)_3^{4-}$	0.473 (0.425)	−0.369 (−0385)	−0.254 (−0.272)	0.417 (0.403)	−0.396 (−0.415)	−0.248 (−0.279)
$PuO_2(C_2O_4)$	0.973 (1.244)	−0.338 (−0.269)	−0.190 (−0.230)	0.724 (0.955)	−0.281 (−0.178)	−0.142 (−0.199)
$PuO_2(C_2O_4)_2^{2-}$	0.711 (0.752)	−0.357 (−0.352)	−0.273 (−0.276)	0.636 (0.647)	−0.377 (−0.366)	−0.269 (−0.268)
$PuO_2(C_2O_4)_3^{4-}$	0.606 (0.578)	−0.377 (−0.381)	−0.274 (−0.293)	0.630 (0.632)	−0.416 (−0.422)	−0.286 (−0.312)
$AmO_2(C_2O_4)$	0.932 (1.203)	−0.301 (−0.231)	−0.196 (−0.230)	0.676 (0.909)	−0.234 (−0.135)	−0.154 (−0.202)
$AmO_2(C_2O_4)_2^{2-}$	0.677 (0.716)	−0.326 (−0.316)	−0.274 (−0.277)	0.593 (0.604)	−0.337 (−0.322)	−0.273 (−0.272)
$AmO_2(C_2O_4)_3^{4-}$	0.580 (0.552)	−0.347 (−0.344)	−0.277 (−0.279)	0.592 (0.591)	−0.378 (−0.375)	−0.290 (−0.314)
			ISOMERS B			
$UO_2(C_2O_4)_3^{4-}$	0.557 (0.519)	−0.374 (−0.385)	−0.266 (−0.272)	0.498 (0.477)	−0.395 (−0.409)	−0.273 (−0.280)
$NpO_2(C_2O_4)_3^{4-}$	0.497 (0.459)	−0.346 (−0.355)	−0.264 (−0.270)	0.430 (0.410)	−0.360 (−0.372)	−0.270 (−0.279)
$PuO_2(C_2O_4)_3^{4-}$	0.643 (0.610)	−0.347 (−0.351)	−0.281 (−0.289)	0.656 (0.635)	−0.374 (−0.381)	−0.298 (−0.308)
$AmO_2(C_2O_4)_3^{4-}$	0.590 (0.559)	−0.332 (−0.333)	−0.278 (−0.287)	0.596 (0.581)	−0.356 (−0.360)	−0.295 (−0.305)

DOI: 10.1021/acs.inorgchem.8b03538
Inorg. Chem. 2019, 58, 3425−3434

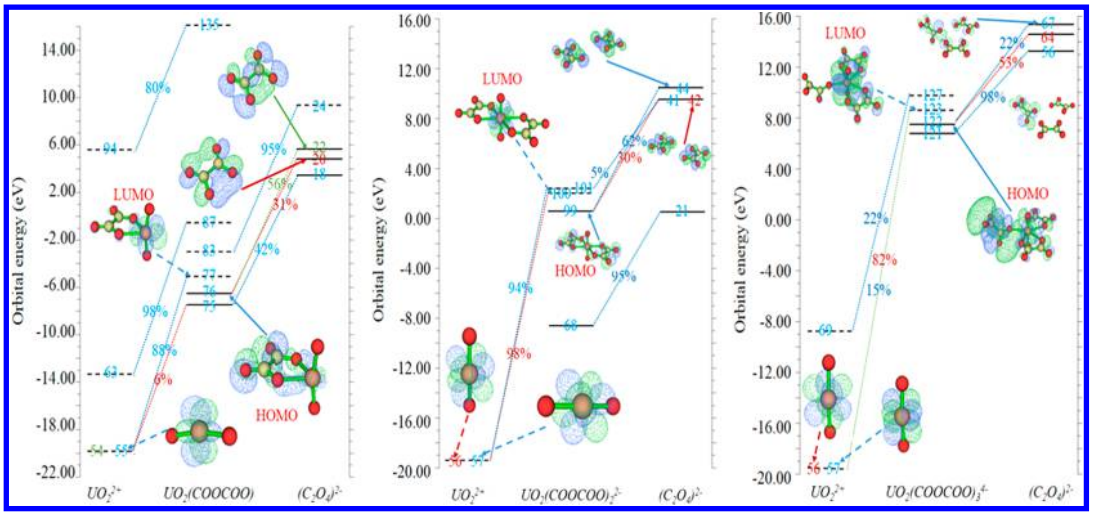

Figure 4. Orbital interaction diagram for $[UO_2(C_2O_4)_n]^{(2n-2)-}$ (n = 1−3). Solid and dashed bars correspond to occupied and virtual MOs, respectively.

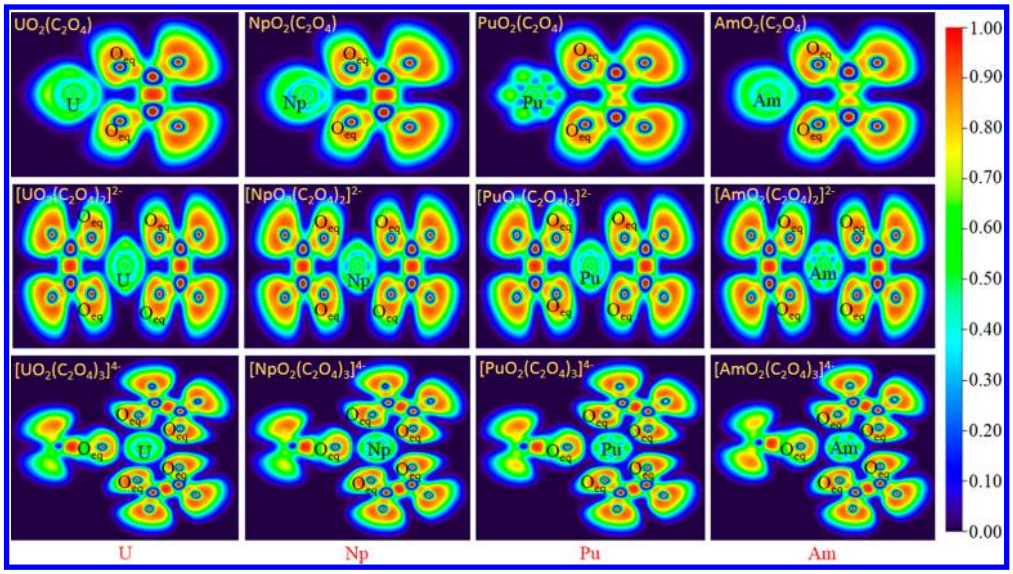

Figure 5. Two-dimensional color-filled plane map of ELF. The results are based on the PW91-ZORA/def2-TZVPP-SARC.

The ELF shaded-surface-projection maps are displayed in Figure 5. The disynaptic valence basins, corresponding to conventional two-center bonds,[62] can be qualitatively described the strength of interatomic interaction. As can be seen, these are unobvious disynaptic valence basins between the An and O_{eq} atoms, which reveals that An−O_{eq} bonds have weak covalent properties. All Mayer bond orders of An−O_{eq} are less than 1, but the corresponding Fuzzy bond orders are higher. For U and Np, the Mayer bond order of An−O_{eq} displays a trend of $AnO_2(C_2O_4)$ > $[AnO_2(C_2O_4)_2]^{2-}$ > $[AnO_2(C_2O_4)_3]^{4-}$, whereas a trend of $AnO_2(C_2O_4)$ < $[AnO_2(C_2O_4)_2]^{2-}$ > $[AnO_2(C_2O_4)_3]^{4-}$ is represented for Pu and Am. It may be attributed to the change of An−O_{eq} bond distances. What's more, the trend of An−O_{eq} bond orders is in parallel with the values of ELF, and all corresponding ELF values appear in Table 4. This phenomenon further confirms that the An−O_{eq} bonds are dominated by ionic interaction.

Topological analyses of the (3, −1) bond-critical points (BCPs) for the An−O_{yl} and An−O_{eq} bonds were listed in Table 3 with the QTAIM theory. Notably, the QTAIM method is a successful strategy to analyze bonding features in actinide complexes.[63,64]

Previous studies[65] have shown that the criterion of total energy density $H(r)$ proposed by Cremer and Kraka[66] can correctly describe the properties of chemical bonds for heavy elemental systems. The $H(r)$ is the sum of the local kinetic energy density $G(r)$ and the local potential energy density $V(r)$. Generally, the properties of chemical bonds can be defined as follows: the value of $H(r)$ is more negative while the covalent interaction is more obvious. Another useful criterion is the $-V(r)/G(r)$ ratio; $-V(r)/G(r) < 1$ is feature of a classical ionic bond, $-V(r)/G(r) > 2$ is diagnostic of a typical covalent interaction, and $1 < -V(r)/G(r) < 2$ can be described as partially covalent bonds.

Topological parameters of An−O_{eq} and An−O_{yl} are listed in Table 4. All $H(r)$ values of calculated BCPs in the $[AnO_2(C_2O_4)_n]^{(2n-2)-}$ complexes are negative. For the An−O_{eq} bond, a low $\rho(r)$ value and a positive $\nabla^2\rho(r)$ value confirm its closed-shell interaction. Meanwhile, it should be noted that the An−O_{eq} bonds have negative $H(r)$ values with small absolute quantities and the ratios of $-V(r)/G(r)$ range from 1

DOI: 10.1021/acs.inorgchem.8b03538
Inorg. Chem. 2019, 58, 3425−3434

Table 4. Topological Parameters for the An−O_{yl} and An−O_{eq} Bond Critical Points (BCPs) in the $[AnO_2(L)_n]^{(2n-2)-}$ (L = (C_2O_4), n = 1−3) Complexes

Species	Bond	$\rho(r)$	$\nabla^2\rho$	$G(r)$	$V(r)$	$H(r)$	$-V(r)/G(r)$	ELF
$UO_2(L)$	U−O_{yl}	0.299	0.370	0.347	−0.601	−0.254	1.732	
	U−O_{eq}	0.062	0.253	0.069	−0.074	−0.006	1.072	0.293
$UO_2(L)_2^{2-}$	U−O_{yl}	0.273	0.362	0.311	−0.532	−0.221	1.711	
	U−O_{eq}	0.080	0.250	0.177	−0.091	−0.014	1.182	0.235
$UO_2(L)_3^{4-}$	U−O_{yl}	0.271	0.364	0.308	−0.525	−0.217	1.721	
	U−O_{eq}	0.059	0.195	0.055	−0.061	−0.006	1.109	0.182
$NpO_2(L)$	Np−O_{yl}	0.304	0.340	0.353	−0.622	−0.268	1.762	
	Np−O_{eq}	0.116	0.371	0.125	−0.158	−0.032	1.264	0.283
$NpO_2(L)_2^{2-}$	Np−O_{yl}	0.282	0.357	0.322	−0.554	−0.233	1.720	
	Np−O_{eq}	0.079	0.256	0.077	−0.090	−0.013	1.169	0.229
$NpO_2(L)_3^{4-}$	Np−O_{yl}	0.279	0.357	0.318	−0.546	−0.228	1.717	
	Np−O_{eq}	0.057	0.191	0.053	−0.058	−0.005	1.094	0.172
$PuO_2(L)$	Pu−O_{yl}	0.302	0.328	0.345	−0.608	−0.263	1.762	
	Pu−O_{eq}	0.065	0.265	0.073	−0.079	−0.007	1.082	0.150
$PuO_2(L)_2^{2-}$	Pu−O_{yl}	0.288	0.373	0.332	−0.570	−0.238	1.717	
	Pu−O_{eq}	0.076	0.260	0.076	−0.088	−0.012	1.158	0.210
$PuO_2(L)_3^{4-}$	Pu−O_{yl}	0.284	0.374	0.324	−0.555	−0.231	1.713	
	Pu−O_{eq}	0.051	0.180	0.048	−0.052	−0.003	1.083	0.151
$AmO_2(L)$	Am−O_{yl}	0.299	0.370	0.347	−0.602	−0.255	1.735	
	Am−O_{eq}	0.063	0.259	0.071	−0.076	−0.006	1.070	0.143
$AmO_2(L)_2^{2-}$	Am−O_{yl}	0.289	0.397	0.335	−0.572	−0.236	1.707	
	Am−O_{eq}	0.075	0.257	0.075	−0.086	−0.011	1.146	0.206
$AmO_2(L)_3^{4-}$	Am−O_{yl}	0.283	0.400	0.326	−0.552	−0.226	1.693	
	Am−O_{eq}	0.048	0.172	0.045	−0.048	−0.002	1.066	0.138
				ISOMERS B				
$UO_2(L)_3^{4-}$	U−O_{yl}	0.277	0.367	0.320	−0.548	−0.228	1.712	
	U−O_{eq}	0.051	0.146	0.042	−0.047	−0.005	1.119	0.187
$NpO_2(L)_3^{4-}$	Np−O_{yl}	0.288	0.361	0.332	−0.574	−0.242	1.729	
	Np−O_{eq}	0.049	0.146	0.041	−0.045	−0.004	1.097	0.181
$PuO_2(L)_3^{4-}$	Pu−O_{yl}	0.291	0.383	0.339	−0.582	−0.243	1.717	
	Pu−O_{eq}	0.047	0.147	0.040	−0.044	−0.003	1.100	0.160
$AmO_2(L)_3^{4-}$	Am−O_{yl}	0.288	0.403	0.337	−0.573	−0.236	1.700	
	Am−O_{eq}	0.044	0.142	0.038	−0.041	−0.003	1.079	0.149

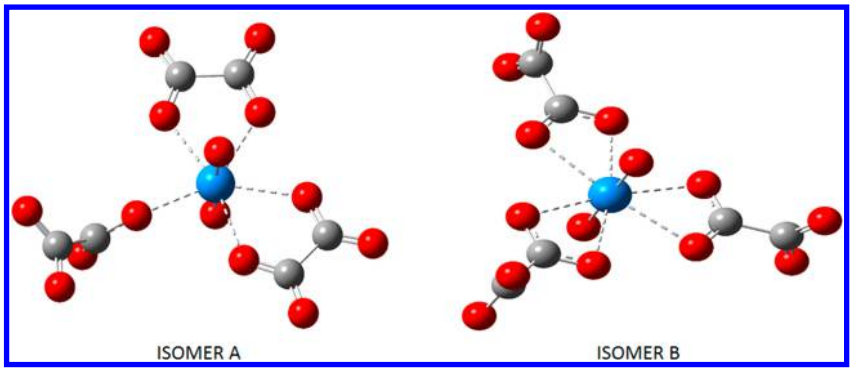

Figure 6. Computed structures of the $[AnO_2(C_2O_4)_3]^{4-}$ complexes using PW91-ZORA/def2-TZVPP-SARC.

to 2, which shows that these bonds have a certain degree of covalent character. This conclusion is consistent with the results of previous charge and ELF analysis. For the An−O_{yl} bonds, all the $H(r)$ values are more negative than An−O_{eq} and the $-V(r)/G(r)$ ratios are closed to 2, which infers that the An−O_{yl} bonds are typical covalent bonds.

3.3. Comparison of Isomers A and Isomers B. Geometric optimization results indicate that there are two specific isomers of $[AnO_2(C_2O_4)_3]^{4-}$ complexes. Their energies are extremely close to each other and are lower than other isomers. In terms of structural characteristics, one is a pentagonal bipyramidal structure (named isomer A) and the other is a hexagonal bipyramidal structure with D_{3h} symmetry (named isomer B). The corresponding structures are depicted in Figure 6. In order to examine the energy order, the higher level PWPB95 with D3BJ was used, and the values were collected in Table S6. The final result shows that the structure of the lowest energy varies with environmental conditions. In the gas phase, Isomers B is the lowest energy structure, while in the solvation model, isomers A is the lowest one. Here, we just take the compounds of the gas phase into account. In view of

DOI: 10.1021/acs.inorgchem.8b03538
Inorg. Chem. 2019, 58, 3425−3434

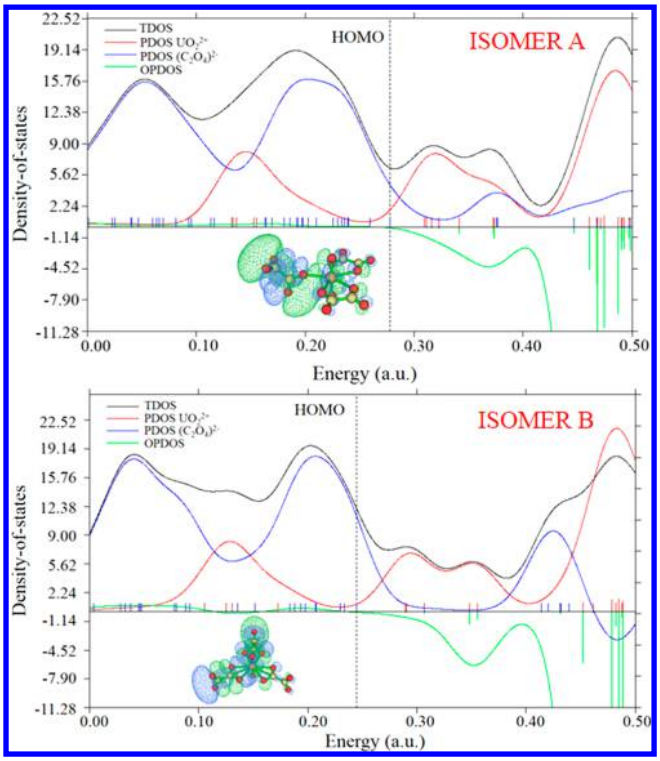

Figure 7. TDOS, PDOS, and OPDOS curves of $[UO_2(C_2O_4)_3]^{4-}$ complexes at the PW91-ZORA/def2-TZVPP-SARC.

this particularity, we separately analyze the similarities and differences between these two structures.

In terms of structural parameters (Table 1), the average bond lengths of An−O_{eq} in isomers B are relatively longer than those in isomers A. The average Hirfsheld charges (Table 3) of An (An = U−Am) and O_{eq} in isomers B have larger absolute quantities than in the isomers A, and the average Mayer bond orders (Table S5) of An−O_{eq} display the same trend. Meanwhile, the bond order appears with a trend of U > Np > Pu > Am.

The topological analysis indicates that the An−O_{eq} bonds of these two structures have the same properties. The values of $H(r)$ are negative, and the results of $-V(r)/G(r)$ ratios are also between 1 and 2. The only difference is that ratios of isomers B are slightly larger than those in the isomers A.

In order to get more in-depth information about orbital interactions in the isomers A and isomers B, the TDOS, PDOS, and OPDOS were calculated and plotted with Gaussian curves. The corresponding full width at half-maximum (fwhm) is 0.05 au. Figure 7 shows the TDOS, PDOS, and OPDOS graphics of the $[UO_2(C_2O_4)_3]^{4-}$ complexes. Fragment 1 is defined as $(UO_2)^{2+}$ orbitals, and fragment 2 is defined as $(C_2O_4)^{2-}$ orbitals. As can be seen, the curve shapes of the DOS are similar in the isomer A and isomer B. At the position of the HOMO energy level (vertical dashed line), the PDOS of $(C_2O_4)^{2-}$ orbitals approached the TDOS, which means that most of the contributions to HOMO result from the $(C_2O_4)^{2-}$ orbitals. The OPDOS values of $(UO_2)^{2+}$ and $(C_2O_4)^{2-}$ are close to zero, which reveals that the interaction between the $(UO_2)^{2+}$ and $(C_2O_4)^{2-}$ is weak. The orbital interactions analysis to the other actinyls complexes can be found in the Supporting Information (Figure S3−S5).

The electrostatic potential (ESP) values of van der Waals (vdW) surfaces were analyzed in order to evaluate the adsorption sites of fission product cations on these actinide organic complexes. The ESP on the vdW surface has been demonstrated by means of an applicable method for detecting intermolecular interaction.[67] Here, we take $[UO_2(C_2O_4)_3]^{4-}$ complexes as examples; the results are shown in Figure 8. The more negative the ESP site, the easier it is to attract electrophiles, while the more positive the ESP site, the easier it is to attract nucleophiles.[68] It can be seen from Figure 8 that the predominate adsorption sites are located at the most negative ESP value of the $[UO_2(C_2O_4)_3]^{4-}$ complex, which occurs between the adjacent oxalates. The adsorption sites of other $[AnO_2(C_2O_4)_n]^{(2n-2)-}$ complexes are similar to $[UO_2(C_2O_4)_3]^{4-}$; the detailed images are displayed in the Supporting Information. The conclusions of adsorption sites were based solely on the electrostatic potential, and the sterically crowded environment will also influence the adsorption properties (depending on the adsorbing species).

4. CONCLUSIONS

The geometric and electronic structures of the complexes formed by actinyls AnO_2^{2+} (An = U−Am) and oxalate ligands have been systematically investigated by using different quantum chemical methods in gas phase. The main conclusions are as follows:

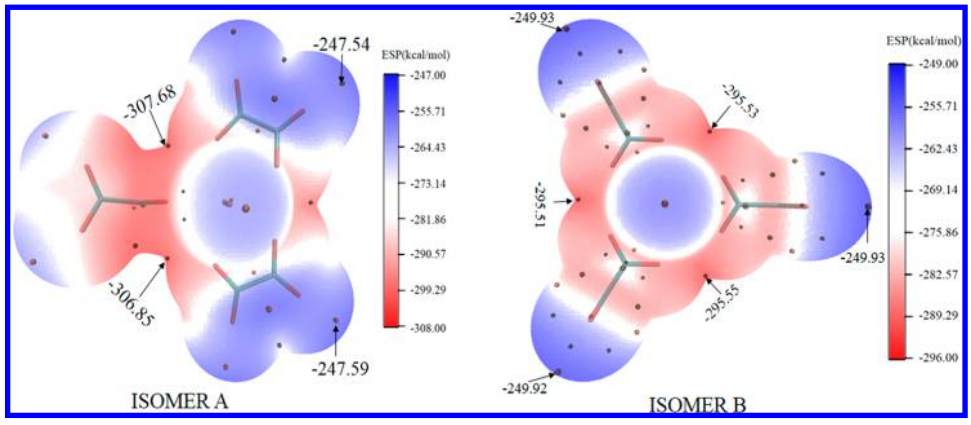

Figure 8. ESP-mapped molecular vdW surfaces of $[UO_2(C_2O_4)_3]^{4-}$ complexes. The unit is in kcal mol^{-1}. Surface local minima and maxima of ESP are represented as black and orange spheres, respectively.

DOI: 10.1021/acs.inorgchem.8b03538
Inorg. Chem. 2019, 58, 3425−3434

(1) The ground state of $[AnO_2(C_2O_4)_n]^{(2n-2)-}$ (An = U, Np, Pu, Am; n = 1−3) was located. Our computational analyses show that all the ground state structures are similar. The O_{eq} atoms prefer to coordinate with the actinyls on the equatorial plane.

(2) The properties of the chemical bonding of $[AnO_2(C_2O_4)_n]^{(2n-2)-}$ complexes were evaluated with electron density difference, CDA, population analysis, bond order analysis, ELF, and QTAIM. The An−O_{eq} dative bonding is an ionic bond with the extent of covalent interaction, and An−O_{yl} bonds are typical covalent bonds.

(3) The DOS approach was implemented to analyze the orbital interactions in the $[AnO_2(C_2O_4)_3]^{4-}$ complexes. The TDOS results show that the HOMO of $[AnO_2(C_2O_4)_3]^{4-}$ primarily comes from $(C_2O_4)^{2-}$ orbitals. The OPDOS analyses suggest that the interaction between the $(AnO_2)^{2+}$ and $(C_2O_4)^2$ is weak. Reactivity analysis of ESP on molecules vdW surfaces indicates that the adsorption sites of fission product cations appear between the adjacent oxalate molecules.

■ ASSOCIATED CONTENT

Supporting Information

The Supporting Information is available free of charge on the ACS Publications website at DOI: 10.1021/acs.inorgchem.8b03538.

The excitation energies of $[AnO_2(C_2O_4)_n]^{(2n-2)-}$ complexes at the PW91-ZORA/def2-TZVPP-SARC level, Cartesian coordinates for the $[AnO_2(C_2O_4)_n]^{(2n-2)-}$ complexes at the PW91-ZORA/def2-TZVPP-SARC level of theory, structural parameters calculated by other methods, Mayer Bond Order (MBO) and Fuzzy Bond Order (FBO) values, relative energies between the isomers A and isomers B, contour plots of the electron density difference, orbital interaction diagram, DOS curves, and ESP mapping molecular vdW surface (PDF)

■ AUTHOR INFORMATION

Corresponding Author

*E-mail: lip@sxu.edu.cn.

ORCID

Peng Li: 0000-0001-8868-9743

Notes

The authors declare no competing financial interest.

■ ACKNOWLEDGMENTS

This work is supported by National Natural Science Foundation of China (NSFC) (Grant No. 11604187), the Natural Science Young Foundation of Shanxi Province (Grant No. 201801D221004), Cooperation projects of Institute of Applied Physics and Computational Mathematics, and Open Fund of Key Laboratory of Advanced Reactor Engineering and Safety, Ministry of Education (Tsinghua University, China). We would like to thank Dr. Sobereva for many helpful discussions and providing us with the Multiwfn package. We are very grateful to the reviewers for the valuable suggestions on improving this work.

■ REFERENCES

(1) Hodge, V. F.; Koide, M.; Goldberg, E. D. Particulate uranium, plutonium and polonium in the biogeochemistries of the coastal zone. *Nature* **1979**, *277*, 206.

(2) Taylor, R. Reaction: a role for actinide chemists. *Chem.* **2016**, *1*, 662−663.

(3) Dresselhaus, M. S.; Thomas, I. L. Alternative energy technologies. *Nature* **2001**, *414*, 332−337.

(4) Ion, S. Reaction: recycling and generation IV systems. *Chem.* **2016**, *1*, 663−665.

(5) Li, J.; Dai, X.; Zhu, L.; Xu, C.; Zhang, D.; Silver, M. A.; Li, P.; Chen, L. H.; Li, Y. Z.; Zuo, D. W.; Zhang, H.; Xiao, C. L.; Chen, J.; Diwu, J.; Farha, O. K.; Albrecht-Schmitt, T. E.; Chai, Z. F.; Wang, S. A. $^{99}TcO_4^-$ remediation by a cationic polymeric network. *Nat. Commun.* **2018**, *9*, 3007.

(6) Kaltsoyannis, N. Does covalency increase or decrease across the actinide series? Implications for minor actinide partitioning. *Inorg. Chem.* **2013**, *52* (7), 3407−3413.

(7) Neidig, M. L.; Clark, D. L.; Martin, R. L. Covalency in f-element Complexes. *Coord. Chem. Rev.* **2013**, *257* (2), 394−406.

(8) Go, Y. B.; Wang, X. Q.; Jacobson, A. J. (6,3)-Honeycomb Structures of Uranium(VI) Benzenedicarboxylate Derivatives: The Use of Noncovalent Interactions to Prevent Interpenetration. *Inorg. Chem.* **2007**, *46* (16), 6594−6600.

(9) Borkowski, L. A.; Cahill, C. L. Topological Evolution in Uranyl Dicarboxylates: Synthesis and Structures of One-Dimensional $UO_2(C_6H_8O_4)(H_2O)_2$ and Three-Dimensional $UO_2(C_6H_8O_4)$. *Inorg. Chem.* **2003**, *42* (22), 7041−7045.

(10) Kim, J. − Y.; Norquist, A. J.; O' Hare, D. Incorporation of uranium(VI) into metal-organic framework solids, $[UO_2(C_4H_4O_4)].H_2O$, $[UO_2F(C_5H_6O_4)].2H_2O$, and $[(UO_2)_{1.5}(C_8H_4O_4)_2]_2[(CH_3)_2NCOH_2].H_2O$. *Dalton Trans.* **2003**, *0*, 2813−2814.

(11) Deria, P.; Gómez-Gualdrón, D. A.; Bury, W.; Schaef, H. T.; Wang, T. C.; Thallapally, P. K.; Sarjeant, A. A.; Snurr, R. Q.; Hupp, J. T.; Farha, O. K. Ultraporous, water stable, and breathing zirconium-based metal-organic frameworks with ftw topology. *J. Am. Chem. Soc.* **2015**, *137*, 13183−13190.

(12) Ramaswamy, P.; Wong, N. E.; Gelfand, B. S.; Shimizu, G. K. H. A water stable magnesium MOF that conducts protons over 10^{-2} S cm^{-1}. *J. Am. Chem. Soc.* **2015**, *137*, 7640−7643.

(13) Jiang, H.-L.; Feng, D.; Wang, K.; Gu, Z.-Y.; Wei, Z.; Chen, Y.-P.; Zhou, H.-C. An exceptionally stable, porphyrinic Zr metal-organic framework exhibiting pH-dependent fluorescence. *J. Am. Chem. Soc.* **2013**, *135*, 13934−13938.

(14) Wang, Y.; Liu, Z.; Li, Y.; Bai, Z.; Liu, W.; Wang, Y.; Xu, X.; Xiao, C.; Sheng, D.; Diwu, J.; Su, J.; Chai, Z.; Albrecht-Schmitt, T. E.; Wang, S. Umbellate distortions of the uranyl coordination environment result in a stable and porous polycatenated framework that can effectively remove cesium from aqueous solutions. *J. Am. Chem. Soc.* **2015**, *137*, 6144−6147.

(15) Wang, Y.; Yin, X.; Liu, W.; Xie, J.; Chen, J.; Silver, M. A.; Sheng, D.; Chen, L.; Diwu, J.; Liu, N.; Chai, Z.; Albrecht-Schmitt, T. E.; Wang, S. Emergence of Uranium as a Distinct Metal Center for Building Intrinsic X-ray Scintillators. *Angew. Chem., Int. Ed.* **2018**, *57*, 7883−7887.

(16) Alsobrook, A. N.; Hauser, B. G.; Hupp, J. T.; Alekseev, E. V.; Depmeier, W.; Albrecht-Schmitt, T. E. Cubic and rhombohedral heterobimetallic networks constructed from uranium, transition metals, and phosphonoacetate: new methods for constructing porous materials. *Chem. Commun.* **2010**, *46*, 9167−9169.

(17) Mihalcea, I.; Henry, N.; Bousquet, T.; Volkringer, C.; Loiseau, T. Six-Fold coordinated uranyl cations in extended coordination polymers. *Cryst. Growth Des.* **2012**, *12*, 4641−4648.

(18) Dognon, J. P.; Clavaguéra, C.; Pyykkö, P. A Predicted Organometallic Series Following a 32-Electron Principle: An@C_{28} (An = Th, Pa^+, U^{2+}, Pu^{4+}). *J. Am. Chem. Soc.* **2009**, *131* (1), 238−243.

(19) Xie, J.; Wang, Y. X.; Liu, W.; Yin, X. M.; Chen, L. H.; Zou, Y. M.; Diwu, J.; Chai, Z. F.; Albrecht-Schmitt, T. E.; Liu, G. K.; Wang, S.

DOI: 10.1021/acs.inorgchem.8b03538
Inorg. Chem. 2019, 58, 3425−3434

A. Highly Sensitive Detection of Ionizing Radiations by a Photoluminescent Uranyl Organic Framework. *Angew. Chem., Int. Ed.* **2017**, *56* (26), 7500−7504.
(20) Dau, P. D.; Wilson, R. E.; Gibson, J. K. Elucidating Protactinium Hydrolysis: The Relative Stabilities of $PaO_2(H_2O)^+$ and $PaO(OH)_2^+$. *Inorg. Chem.* **2015**, *54* (15), 7474−7480.
(21) Kaltsoyannis, N. Covalency Hinders $AnO_2(H_2O)^+ \rightarrow AnO(OH)_2^+$ Isomerisation (An= Pa-Pu). *Dalton Trans.* **2016**, *45* (7), 3158−3162.
(22) Vasiliu, M.; Peterson, K. A.; Gibson, J. K.; Dixon, D. A. Reliable Potential Energy Surfaces for the Reactions of H_2O with ThO_2, PaO_2^+, UO_2^{2+}, and UO_2^+. *J. Phys. Chem. A* **2015**, *119* (46), 11422−11431.
(23) Wen, X.-D.; Martin, R. L.; Roy, L. E.; Scuseria, G. E.; Rudin, S. P.; Batista, E. R.; McCleskey, T. M.; Scott, B. L.; Bauer, E.; Joyce, J. J.; Durakiewicz, T. Effect of Spin-Orbit Coupling on the Actinide Dioxides AnO_2 (An= Th, Pa, U, Np, Pu, and Am): A Screened Hybrid Density Functional Study. *J. Chem. Phys.* **2012**, *137* (15), 154707.
(24) Polinski, M. J.; Wang, S.; Alekseev, E. V.; Depmeier, W.; Liu, G.; Haire, R. G.; Albrecht-Schmitt, T. E. Curium (III) borate shows coordination environments of both Plutonium (III) and Americium (III) borates. *Angew. Chem., Int. Ed.* **2012**, *51* (8), 1869−1872.
(25) Minasian, S. G.; Boland, K. S.; Feller, R. K.; Gaunt, A. J.; Kozimor, S. A.; May, I.; Reilly, S. D.; Scott, B. L.; Shuh, D. K. Synthesis and Structure of $(Ph_4P)_2MCl_6$ (M = Ti, Zr, Hf, Th, U, Np, Pu). *Inorg. Chem.* **2012**, *51* (10), 5728−5736.
(26) Schnaars, D. D.; Wilson, R. E. Synthesis, Structure, and Vibrational Properties of $[Ph_4P]_2NpO_2Cl_4$ and $[Ph_4P]_2PuO_2Cl_4$ Complexes. *Inorg. Chem.* **2018**, *57* (6), 3008−3016.
(27) Hu, S.-X.; Li, W.-L.; Dong, L.; Gibson, J. K.; Li, J. Crown ether complexes of actinyls: A computational assessment of AnO_2(15-crown-5)$^{2+}$ (An = U, Np, Pu, Am, Cm). *Dalton Trans.* **2017**, *46* (36), 12354−12363.
(28) Hu, S. − X.; Liu, J. − J.; Gibson, J. K.; Li, J. Periodic Trends in Actinyl Thio-Crown Ether Complexes. *Inorg. Chem.* **2018**, *57* (5), 2899−2907.
(29) Neese, F. The ORCA program system. Comput. *Mol. Sci.* **2012**, *2* (1), 73−78.
(30) Perdew, J. P.; Burke, K.; Wang, Y. Generalized gradient approximation for the exchange-correlation hole of a many-electron system. *Phys. Rev. B: Condens. Matter Mater. Phys.* **1996**, *54*, 16533.
(31) Becke, A. D. Density-functional thermochemistry. III. The role of exact exchange. *J. Chem. Phys.* **1993**, *98*, 5648−5652.
(32) Goerigk, L.; Grimme, S. Efficient and Accurate Double-Hybrid-Meta-GGA Density Functionals-Evaluation with the Extended GMTKN30 Database for General Main Group Thermochemistry, Kinetics, and Noncovalent Interactions. *J. Chem. Theory Comput.* **2011**, *7*, 291−309.
(33) Grimme, S.; Antony, J.; Ehrlich, S.; Krieq, H. A consistent and accurate ab initio parametrization of density functional dispersion correction (DFT-D) for the 94 elements H-Pu. *J. Chem. Phys.* **2010**, *132*, 154104.
(34) Pantazis, D. A.; Neese, F. All-Electron scalar relativistic basis sets for the actinides. *J. Chem. Theory Comput.* **2011**, *7*, 677−684.
(35) Pantazis, D. A.; Chen, X. Y.; Landis, C. R.; Neese, F. All-electron scalar relativistic basis sets for third-row transition metal atoms. *J. Chem. Theory Comput.* **2008**, *4*, 908−919.
(36) Rappoport, D.; Furche, F. Property-optimized Gaussian basis sets for molecular response calculations. *J. Chem. Phys.* **2010**, *133*, 134105.
(37) Van Lenthe, E.; Baerends, E. J.; Snijders, J. C. Relativistic regular two-component Hamiltonians. *J. Chem. Phys.* **1993**, *99*, 4597.
(38) Hess, B. A. Relativistic electronic-structure calculations employing a two-component no-pair formalism with external-field projection. *Phys. Rev. A: At., Mol., Opt. Phys.* **1986**, *33*, 3742.
(39) Jansen, G.; Hess, B. A. Revision of Douglas-Kroll transformation. *Phys. Rev. A: At., Mol., Opt. Phys.* **1989**, *39*, 6016.
(40) Klamt, A.; Schüürmann, G. COSMO-A new approach to dielectric screening in solvents with explicit expressions for the screening energy and its gradient. *J. Chem. Soc., Perkin Trans. 2* **1993**, *0* (5), 799−805.
(41) Cao, Z. J.; Balasubramanian, K. Theoretical studies of $UO_2(OH)(H_2O)_n^+$, $UO_2(OH)(H_2O)_n$, $NpO_2(OH)(H_2O)_n$ and $PuO_2(OH)(H_2O)_n^+$ ($n \leq 21$) complexes in aqueous solution. *J. Chem. Phys.* **2009**, *131*, 164504.
(42) Rios, D.; Michelini, M. C.; Lucena, A. F.; Marçalo, J.; Bray, T. H.; Gibson, J. K. Gas-Phase Uranyl, Neptunyl, and Plutonyl: Hydration and Oxidation Studied by Experiment and Theory. *Inorg. Chem.* **2012**, *51*, 6603−6614.
(43) Lu, T.; Chen, F. W. Multiwfn: A multifunctional wavefunction analyzer. *J. Comput. Chem.* **2012**, *33*, 580−592.
(44) Dapprich, S.; Frenking, G. Investigation of Donor-Acceptor Interactions: A Charge Decomposition Analysis Using Fragment Molecular Orbitals. *J. Phys. Chem.* **1995**, *99*, 9352−9362.
(45) Hirshfeld, F. L. Bonded-Atom Fragments for Describing Molecular Charge Densities. *Theoret. Chim. Acta* **1977**, *44*, 129−138.
(46) Fonseca Guerra, C.; Handgraaf, J. W.; Baerends, E. J.; Bickelhaupt, F. M. Voronoi Deformation Density (VDD) Charges: Assessment of the Mulliken, Bader, Hirshfeld, Weinhold, and VDD Methods for Charge analysis. *J. Comput. Chem.* **2004**, *25*, 189−210.
(47) Mayer, I. Charge, bond order and valence in the ab initio SCF theory. *Chem. Phys. Lett.* **1983**, *97* (3), 270−274.
(48) Nalewajski, R. F.; Mrozek, J. Modified valence indices from the two-particle density matrix. *Int. J. Quantum Chem.* **1994**, *51* (4), 187−200.
(49) Nalewajski, R. F.; Mrozek, J.; Michalak, A. Two-electron valence indices from the Kohn-Sham orbitals. *Int. J. Quantum Chem.* **1997**, *61* (3), 589−601.
(50) Michalak, A.; DeKock, R. L.; Ziegler, T. Bond multiplicity in transition-metal complexes: applications of two-electron valence indices. *J. Phys. Chem. A* **2008**, *112* (31), 7256−7263.
(51) Mitoraj, M.; Michalak, A. Natural orbitals for chemical valence as descriptors of chemical bonding in transition metal complexes. *J. Mol. Model.* **2007**, *13* (2), 347−355.
(52) de Silva, P.; Korchowiec, J.; Wesolowski, T. A. Revealing the Bonding Pattern from the Molecular Electron Density Using Single Exponential Decay Detector: An Orbital-Free Alternative to the Electron Localization Function. *ChemPhysChem* **2012**, *13* (15), 3462−3465.
(53) Bader, R. W. B. *Atoms in Molecules: A Quantum Theory*; Oxford University Press: Oxford, U.K., 1990.
(54) Hoffmann, R. *Solids and surfaces: a chemist's view of bonding in extended structures*; VCH: New York, 1988.
(55) Malecki, J. G. Synthesis, crystal, molecular and electronic structures of thiocyanate ruthenium complexes with pyridine and its derivatives as ligands. *Polyhedron* **2010**, *29*, 1973−1979.
(56) Fu, R.; Lu, T.; Chen, F. Comparing methods for predicting the reactive site of electrophilic substitution. *Acta Physico-Chemica Sinica* **2014**, *30*, 628.
(57) Pyykkö, P. Additive covalent radii for single-, double-, and triple-bonded molecules and tetrahedrally bonded crystals: A summary. *J. Phys. Chem. A* **2015**, *119* (11), 2326−2337.
(58) Li, J.; Bursten, B. E. Electronic structure of cycloheptatrienyl sandwich compounds of actinides: $An(\eta^7\text{-}C_7H_7)_2$ (An = Th, Pa, U, Np, Pu, Am). *J. Am. Chem. Soc.* **1997**, *119* (38), 9021−9032.
(59) Hu, S. X.; Gibson, J. K.; Li, W. L.; Van Stipdonk, M. J.; Martens, J.; Berden, G.; Redlich, B.; Oomens, J.; Li, J. Electronic structure and characterization of a uranyl di-15-crown-5 complex with an unprecedented sandwich structure. *Chem. Commun.* **2016**, *52* (86), 12761−12764.
(60) Liu, J.-B.; Chen, G. P.; Huang, W.; Clark, D. L.; Schwarz, W. H. E.; Li, J. Bonding trends across the series of tricarbonato-actinyl anions $[(AnO2)(CO3)3]^{4-}$ (An = U-Cm): the plutonium turn. *Dalton Trans.* **2017**, *46*, 2542−2550.
(61) Tassell, M. J.; Kaltsoyannis, N. Covalency in AnCp4 (An = Th-Cm): a comparison of molecular orbital, natural population and

DOI: 10.1021/acs.inorgchem.8b03538
Inorg. Chem. 2019, 58, 3425−3434

atoms-in-molecules analyses. *Dalton Trans.* **2010**, *39* (29), 6719−6725.
(62) Silvi, B. The synaptic order: a key concept to undersrand multicenter bonding. *J. Mol. Struct.* **2002**, *614*, 3−10.
(63) Sajith, P. K.; Suresh, C. H. Mechanisms of Reductive Eliminations in Square Planar Pd(II) Complexes: Nature of Eliminated Bonds and Role of trans Influence. *Inorg. Chem.* **2011**, *50* (17), 8085−8093.
(64) Li, P.; Niu, W. X.; Gao, T. Systematic analysis of structural and topological properties: new insights into $PuO_2(H_2O)_n^{2+}$ (n = 1−6) complexes in the gas phase. *RSC Adv.* **2017**, *4*, 29806.
(65) Farrugia, L. J.; Senn, H. M. Metal-Metal and Metal-Ligand bonding at a QTAIM catastrophe: a combined experimental and theoretical charge density study on the alkylidyne cluster $Fe_3(\mu\text{-H})(\mu\text{-COMe})(CO)_{10}$. *J. Phys. Chem. A* **2010**, *114*, 13418.
(66) Cremer, D.; Kraka, E. Chemical bonds without bonding electron density-does the difference electron-density analysis suffice for a description of the chemical bond? *Angew. Chem., Int. Ed. Engl.* **1984**, *23*, 627.
(67) Murray, J. S.; Politzer, P. The electrostatic potential: an overview. *WIRES Com. Mol. Sci.* **2011**, *1* (2), 153−163.
(68) Lu, T.; Chen, F. Quantitative analysis of molecular surface based on improved Marching Tetrahedra algorithm. *J. Mol. Graphics Modell.* **2012**, *38*, 314−323.

DOI: 10.1021/acs.inorgchem.8b03538
Inorg. Chem. 2019, 58, 3425−3434